Nanoscale Advances

ROYAL SOCIETY OF CHEMISTRY

PAPER

View Article Online
View Journal | View Issue

Cite this: *Nanoscale Adv.*, 2021, **3**, 1106

The improved photocatalytic activity of highly expanded MoS_2 under visible light emitting diodes†

Magdeline Tze Leng Lai,[a] Kian Mun Lee,[a] Thomas Chung Kuang Yang,[b] Guan Ting Pan,[b] Chin Wei Lai,[a] Chia-Yun Chen,[cd] Mohd Rafie Johan[a] and Joon Ching Juan *[ae]

Received 9th November 2020
Accepted 27th December 2020

DOI: 10.1039/d0na00936a

rsc.li/nanoscale-advances

Photocatalytic degradation is a promising method to remove organic pollutants from water. Photocatalysts based on two-dimensional (2D) transition metal dichalcogenides (TMDs) such as MoS_2 nanomaterials have gained tremendous popularity. This is due to their narrow band gap and high visible light absorption. Herein, a MoS_2 photocatalyst with highly expanded interlayer spaces of 1.51 nm was synthesized in the presence of Pluronic F-127 as a template by a facile one-pot hydrothermal method. This expanded MoS_2 (MF-1) managed to photodegrade 98% (2.62×10^{-2} min^{-1}) of methylene blue (MB) dye under irradiation of 1 W visible light-emitting diode (LED) white light. The dominant performance of MF-1 is attributed to the highly expanded interlayer spacing, which exposed more active edge sites. Moreover, the formation of surface defects such as surface cracks and sulfur vacancies (Sv) facilitates the adsorption capacity and *in situ* generation of reactive oxygen species (ROS). The dominant ROS responsible for the photodegradation of MB is superoxide radical ($^{\bullet}O_2^-$). The photocatalyst shows good recyclability without deterioration even after five consecutive cycles.

1. Introduction

The growth of the human population and rapid development of industrial activities has led to environmental pollution. Water pollution is often a result of irresponsible anthropogenic activities. For instance, discharge of untreated dye effluents from the textile industry is a major contributor to water pollution.[1] It is estimated that 200 000 metric tons of wastewater containing harmful organic chemical substances are discharged annually without proper treatment technology.[2] Untreated dye molecules in water bodies may pose substantial threats to aquatic life and human health, as they undergo chemical and biological transformation to toxic substances. According to sustainable development goal (SDG) 2030, clean water and sanitation is a particularly important goal to ensure that drinking water is safe and affordable for people worldwide.[3] Hence, efficient technologies for the removal of water pollutants are greatly desired and anticipated.

In past decades, many methods have been introduced to remove dye pollutants effectively from wastewater, including adsorption,[4] photocatalytic degradation,[5] catalytic oxidation[6] and biological processes.[7] Amongst these, photocatalytic degradation has been widely reported as an efficient and biosafe remedy.[8] This is due to the versatility and sustainability of photocatalysts, which can be activated under the irradiation of natural sunlight to degrade dye molecules.[9] TiO_2 is a traditional photocatalyst that has been actively applied in photocatalytic degradation activity. However, due to its wide band gap of ~3.2 eV, it can only be activated under UV light irradiation.[10] In other words, TiO_2 can only be activated by UV light, which represents approximately less than 5% of solar light. Therefore, many researchers have attempted to tune the band gap of TiO_2 to the visible light-active region or have synthesized new types of photocatalysts.[10] Recently, the usage of an energy-efficient light source such as LED white light has attracted considerable interest than that of visible light from traditional UV lamps or high-power xenon lamps.[11] Although LED light is more energy-efficient, presently, there are only a few reports on the use of LED white light-active photocatalysts such as $ZnO_{0.6}S_{0.4}$,[12] Ag/AgBr,[13] Fe^{3+}-doped g-C_3N_4 (ref. 14) and g-C_3N_4/Nb_2O_5 (ref. 15) for the photodegradation of water pollutants. They are capable of photodegrading organic pollutants within 240 min on irradiation with 3–150 W visible LED light.

MoS_2 nanostructures are a transition metal dichalcogenide (TMD) material that is commonly used as a co-catalyst in the

[a]*Nanotechnology & Catalysis Research Centre, Institute for Advanced Studies, University of Malaya, 50603 Kuala Lumpur, Malaysia. E-mail: jcjuan@um.edu.my*

[b]*Department of Chemical Engineering and Biotechnology, National Taipei University of Technology, Taipei, Taiwan*

[c]*Department of Materials Science and Engineering, National Cheng Kung University, Tainan, 70101, Taiwan*

[d]*Hierarchical Green-Energy Materials (Hi-GEM) Research Center, National Cheng Kung University, Tainan, 70101, Taiwan*

[e]*School of Science, Monash University, Malaysia Campus, Jalan Lagoon Selatan, 46150, Sunway, Selangor, Malaysia*

† Electronic supplementary information (ESI) available. See DOI: 10.1039/d0na00936a

photocatalytic activity.[16,17] However, MoS_2 is a potential candidate in photocatalysis due to its unique physiochemical and optical properties, which can be modified by reducing the MoS_2 staking layer.[18] Generally, bulk MoS_2 is optically inactive and also shows low photoluminescence response due to its indirect band gap of 1.29 eV.[19] Meanwhile, the direct band gap of single or few layers-thick MoS_2 exhibits a peak at 1.8–1.9 eV; therefore, it is a highly suitable semiconductor oxide to be activated within the visible light region.[20] Moreover, with such a narrow band gap, MoS_2 possesses rapid transfer of charge carriers along with wide absorption in the range of visible light; therefore, it is a promising and valuable photocatalyst candidate.[20,21]

Generally, MoS_2 is fabricated based on the tri-atomic-thick regime of S–Mo–S layers, where the Mo atom is located between two trigonal atomic layers of S atom.[22] The bond between Mo and S atom is linked by strong covalent bonds, whereas the interlayer of S–Mo–S is bonded *via* van der Waals forces.[23] The crystalline MoS_2 consists of basal and edge planes, where the former is inherently and thermodynamically favored to have higher surface exposure.[24] Despite this, the photocatalytic activity of MoS_2 is often limited as a result of its dependency on the availability of edge sites.[25] Therefore, many studies have been devoted to improving the exposure of MoS_2 edge sites through morphology control,[26] development of amorphous-state MoS_2 with unsaturated Mo and S sites,[27] surface defects[28] and expansion of the interlayer distance.[29] Generally, the intrinsic structure of MoS_2 has an interlayer spacing of around 0.62 nm.[30] It has been reported that expansion of the interlayer spacing of MoS_2 can reach 0.91 nm. This spacing enabled the expanded MoS_2 to form a composite with CdS nanorods, and the photocatalytic activity was enhanced by 21-fold.[31]

The interaction between the MoS_2 layers is governed by weak van der Waals forces. Upon introduction of foreign substances such as oxygen,[32] soft templates,[22] polymers[33] or carbon,[34] the interlayer spacing of MoS_2 can be expanded. Furthermore, the intercalation of foreign substances indirectly instigates defects in the crystal structure, which can enhance the exposure of the catalyst active sites. For instance, Li *et al.*[22] synthesized expanded MoS_2 with polyethylene glycol (PEG) under a hydrothermal route. Zhou *et al.*[32] synthesized oxygen-incorporated defect-rich MoS_2 nanosheets with expanded interlayers through a solvothermal method. The expanded interlayer spacing that exposes more edge sites manages to improve the performance of MoS_2 for the electrocatalytic activity of the hydrogen evolution reaction (HER). This is because the expansion of the interlayers allows the intercalation of foreign ions, improving the electrochemical performance. However, the photocatalytic activity of the highly expanded interlayer MoS_2 is still very limited.

In this study, highly expanded MoS_2 was successfully synthesized by a facile one-pot hydrothermal method. A Pluronic F-127 surfactant template under acidic conditions was employed to produce highly expanded interlayers of MoS_2. The highly expanded MoS_2 exhibited high photocatalytic performance under 1 W of LED white light irradiation and great reusability.

2. Experimental

Preparation of MoS_2 photocatalyst

A suspension was prepared by mixing 4 mmol of $Na_2MoO_4 \cdot 2H_2O$ [99.5%, Merck] and 8 mmol of C_2H_5NS [99.0%, Merck] in 50 mL of deionized water. Then, the mixture was stirred for 30 min. Subsequently, F-127 (0.4 g) was added to the suspension, and the pH was adjusted to 1, 3, and 5, respectively, with HCl (37%, Merck). The suspensions with pH 1, 3 and 5 are denoted as MF-1, MF-3 and MF-5, respectively. Then, the solution was further stirred for 3 h before being transferred into a Teflon-lined stainless steel autoclave. The autoclave was subjected to hydrothermal treatment at 180 °C for 24 h. After hydrothermal treatment, the precipitate was washed with acetone, ethanol and lastly distilled water several times. For comparison purposes, MoS_2 was synthesized without the addition of F-127 or adjustment of the pH; this sample is denoted as M. Meanwhile, the MoS_2 sample with the addition of F-127 only is denoted as MF.

Photocatalytic degradation experiment

The photocatalytic degradation activity was studied using a custom-made photoreactor with 1 W LED as the light source. The distance between the light source and dye solution is 2 cm. Then, 10 mg of MoS_2 was added to 50 mL of 20 mg L^{-1} MB dye solution and allowed to stir in the dark for 30 min to achieve adsorption–desorption equilibrium. The photodegradation reaction was initiated for 120 min, and 3 mL of suspension was collected at 15 min intervals. The collected suspension was filtered and analyzed using a UV-vis spectrophotometer at a maximum absorption wavelength of 664 nm. The efficiency of the synthesized MoS_2 in the photocatalytic degradation of MB dyes was calculated by eqn (1).

$$\text{Photodegradation efficiency (\%)}: \quad \frac{C_o - C}{C_o} \times 100 \qquad (1)$$

where C_o represents the initial concentration of dye (ppm) and C is the recorded value of the variable reaction concentration (ppm). Chemical oxygen demand (COD) tests were conducted to identify the capacity of the photocatalyst in the mineralization of MB dye.[35] The COD value obtained refers to the amount of oxygen needed by the organic dyes to be oxidized into CO_2 and H_2O species. The chemical oxygen demand (COD) levels before and after degradation of the solution were identified using the APHA Standard Method, whereby the samples were added to COD digestion solution and digested at 150 °C for 2 h. The COD level was then measured using a HACH DR2800 spectrophotometer and the COD removal (%) was calculated based on eqn (2):

$$\text{COD removal (\%)}: \quad \frac{COD_i - COD_f}{COD_i} \times 100 \qquad (2)$$

where COD_i and COD_f are the initial and final concentrations of COD in the pollutant solution, respectively.

Characterization of the MoS_2 samples

The X-ray diffraction (XRD) of the MoS_2 samples was studied using a PANalytical EMPYREAN diffractometer with Cu Kα (λ =

1.54 Å), scanning 2θ in the range of 5–80° and a step size of 0.04° s^{-1}. The *d*-spacings of the samples were calculated using eqn (3).

$$n\lambda = 2d_{hkl} \sin \theta \quad (3)$$

where d_{hkl} represents the perpendicular distances between the *hkl* plates, n is the order of diffraction, λ is the incident ray wavelength and θ is the angle of incidence, also referred to as the angle of scattering. Meanwhile, the crystallite sizes were calculated using the Debye–Scherrer formula (eqn (4)).

$$D = \frac{0.9\lambda}{\beta \cos \theta} \quad (4)$$

where D is the crystallite size, λ is the incident ray wavelength, β is the full width at half maximum (FWHM) and θ refers to the Bragg diffraction angle. The surface morphologies of the MoS_2 samples were observed and captured using a field-emission scanning electron microscope (FESEM, FEI QuantaFEG650 S) with 20 kV radiation. The synthesized sample was mounted on FESEM stubs and coated with a layer of gold. High-resolution images were captured using a high resolution transmission electron microscope (HRTEM, FEI Tecnai G2 F20), operated at an acceleration voltage of 200 kV with 0.2 nm resolution. Raman and photoluminescence (PL) tests were performed using a Renishaw inVia Raman Microscope (Gloucestershire, UK) with 514 nm and 325 nm Ar-ion lasers, respectively. The optical properties of the MoS_2 samples were recorded using an ultraviolet-visible spectrophotometer (UV-Vis, Perkin Elmer Lambda 35 UV-Vis spectrophotometer) from 200–800 nm. The band gaps of the samples were obtained using Tauc's equation (eqn (5)):

$$\alpha h\nu = A(h\nu - E_g)^n \quad (5)$$

where α is the absorption coefficient, $h\nu$ is the photon energy, E_g represents the optical band gap and A is the proportionality constant, which is $n = 2$ for direct transition mode. The chemical and elemental analysis of the samples was performed using a JEOL JPS-9030 X-ray photoelectron spectrometer (XPS, Tokyo, Japan) equipped with an X-ray source of Mg Kα (1253.6 eV). The binding energy of the XPS element peaks obtained was calibrated with the C 1s standard position at 284.2 eV. The procedure for XPS analysis was conducted based on three requirements: (i) the spin–orbit splitting energies of Mo 3d and S2p are fixed to 3.13 ± 0.2 eV and 1.18 ± 0.2 eV, respectively, (ii) the constraint of the FWHM for both peaks in a doublet is fixed to be constant, and (iii) the peak area ratio of the doublet peak is assigned based on the degeneracy of the spin state. The stoichiometric ratios (S/Mo) for the samples were obtained based on the integrated peak area of the ratio of the Mo 3d and S 2p states with the use of relative sensitivity factors (RSF) of 9.5 and 1.67, respectively.

Photoelectrochemical study of the MoS_2 samples

Photoelectrochemical measurements of the samples were performed on a Metrohm Autolab instrument (PGSTAT302N). The electrochemical workstation involved a three-electrode system with the sample coated on fluorine-doped tin oxide glass (1 × 1 cm) as the working electrode, Ag/AgCl as the reference electrode and Pt as the counter electrode. 0.5 M of aqueous Na_2SO_4 at pH 6.5 was used as an electrolyte. The photocurrent test was conducted using a 150 W Xe lamp with an applied bias of 0.2 V. The electrochemical impedance spectroscopy (EIS) was performed

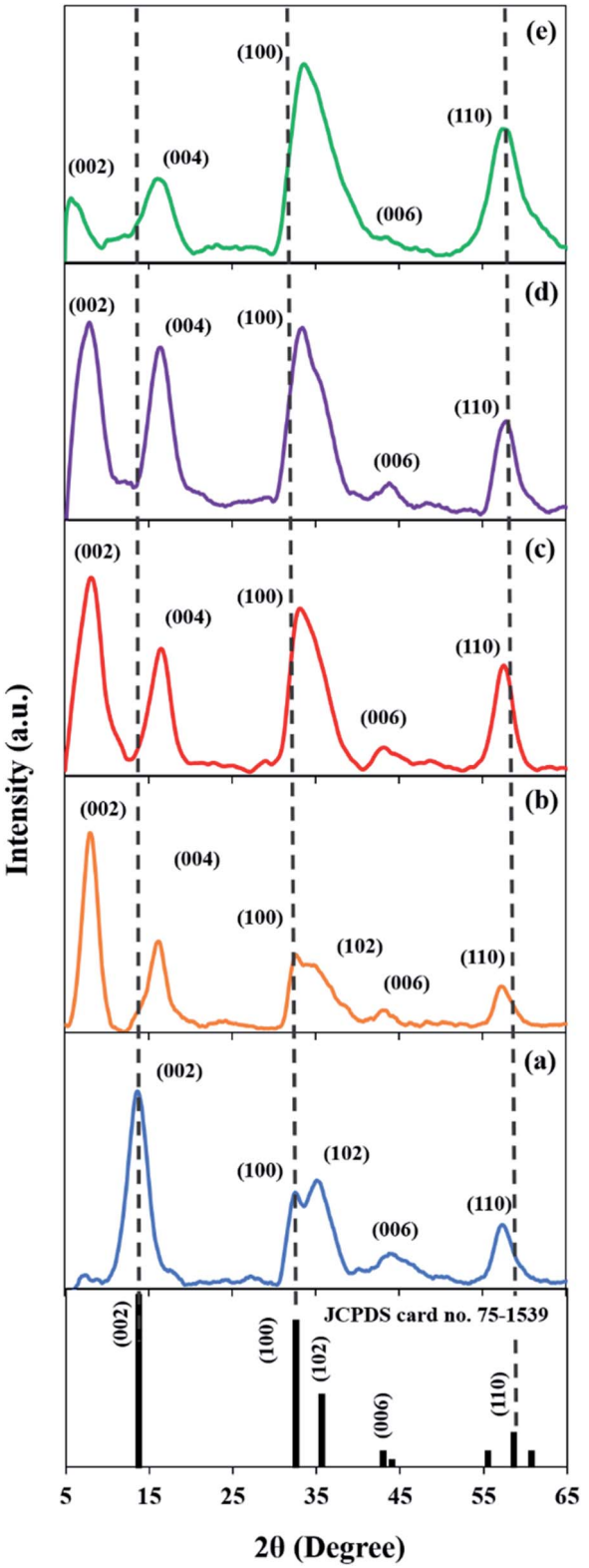

Fig. 1 XRD patterns of (a) M, (b) MF, (c) MF-5, (d) MF-3, and (e) MF-1.

with an AC amplitude of 50 mV and at a frequency of 0.1 Hz to 100 kHz. The Mott–Schottky (M–S) plot of the sample MF-1 was measured in the potential range of −0.4 to 0.8 V (*vs.* Ag/AgCl) with a potential step at 500 Hz frequency. The conversion of the potential *E vs.* Ag/AgCl (pH 6.5) to *E vs.* normal hydrogen electrode (NHE, pH 7.0) was based on eqn (6). The conduction band energy (E_{CB}) was calculated based on eqn (7).[36]

$$E_{NHE,pH\ 7} = E_{(Ag/AgCl,pH\ 6.5)} + \Delta V - 0.059 \times (7.0 - 6.5) \quad (6)$$

$$E_{CB} = E_{VB} - E_g \quad (7)$$

where $\Delta V = 0.21$ V refers to the Ag/AgCl potential against NHE, E_{CB} is the conduction band potential, E_{VB} represents the valence band potential and E_g is the band gap energy (eV).

3. Results and discussion

3.1. XRD analysis

Fig. 1a shows the XRD pattern of the pristine MoS_2 (M), which exhibits a typical diffraction pattern of MoS_2 (JCPDS no. 75-1539). The peaks at 14.2°, 32.1°, 34.9°, 43.7° and 57.0° correspond to the (002), (100), (102), (006) and (110) lattice planes of MoS_2, respectively.[37] A distinctive peak of (002) at 14.2° indicates that the S–Mo–S layers are stacked in an ordered manner.[38] On the other hand, the (002) plane of MF (Fig. 1b) shifted to a lower angle (8.1°). Interestingly, a new peak at 16.2° corresponding to the (004) plane emerged. This suggests that the interlayer spacing of MoS_2 had expanded. This is in concordance with a previous study,[39] in which the peak of the expanded MoS_2 at 14.4° shifted to 8.9° while a new peak at 17.8° corresponding to the (004) plane was observed. The relationship between the peak shifting and the expansion of interlayer spaces was further verified through calculation of the *d*-spacing.

Based on Table 1, the intrinsic *d*-spacing of M is 0.62 nm. Meanwhile, the *d*-spacing of MF is 1.09 nm, which is 1.75 times higher than that of M. This occurrence is due to the intercalation of F-127 surfactant between the crystal lattice, which caused the MoS_2 lattice structure to expand. This was also observed by Chen *et al.*,[40] as the usage of cetyltrimethylammonium bromide (CTAB) surfactant successfully

Table 1 Properties of the synthesized MoS_2 samples

Sample	Interlayer spacing (nm)	Crystallite size (nm)	B/A ratio	S/Mo ratio	Mo^{4+}/Mo^{6+}
M	0.62	13.55	0.57	2.0	—
MF	1.09	3.85	0.59	1.7	3.4
MF-5	1.05	4.86	0.59	1.6	2.4
MF-3	1.07	3.37	0.65	1.7	3.1
MF-1	1.51	3.88	0.66	1.4	1.2

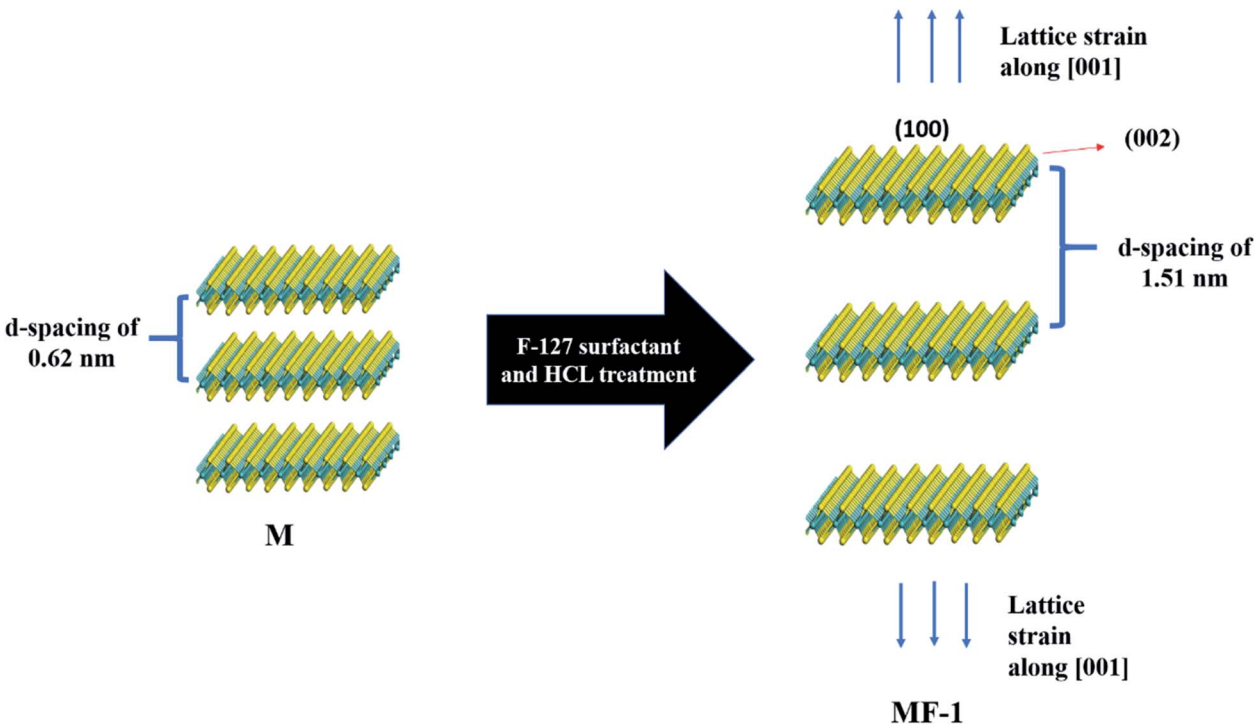

Fig. 2 Schematic of sample M and the expansion of the *d*-spacing of sample MF-1.

expanded the MoS_2 interspacing to 56%. Notably, MF-1 exhibited the largest expanded interlayer spacing of 1.51 nm, which is more than double that of M. This very large lattice expansion will cause MF-1 to undergo uniaxial lattice strain along the [001] direction and thus induces in-plane compression (Fig. 2). It is noteworthy that the (002) peaks of the samples were broadened, indicating changes in the crystallite size. By using the Scherrer equation (eqn (4)), the FWHM for the (002) diffraction peak was calculated (Table 1). It can be observed that the samples with expanded interlayer spacings have much lower crystallite sizes compared to sample M, which also indicates the presence of disordered and shorter-range structures in samples MF, MF-5, MF-3 and MF-1.

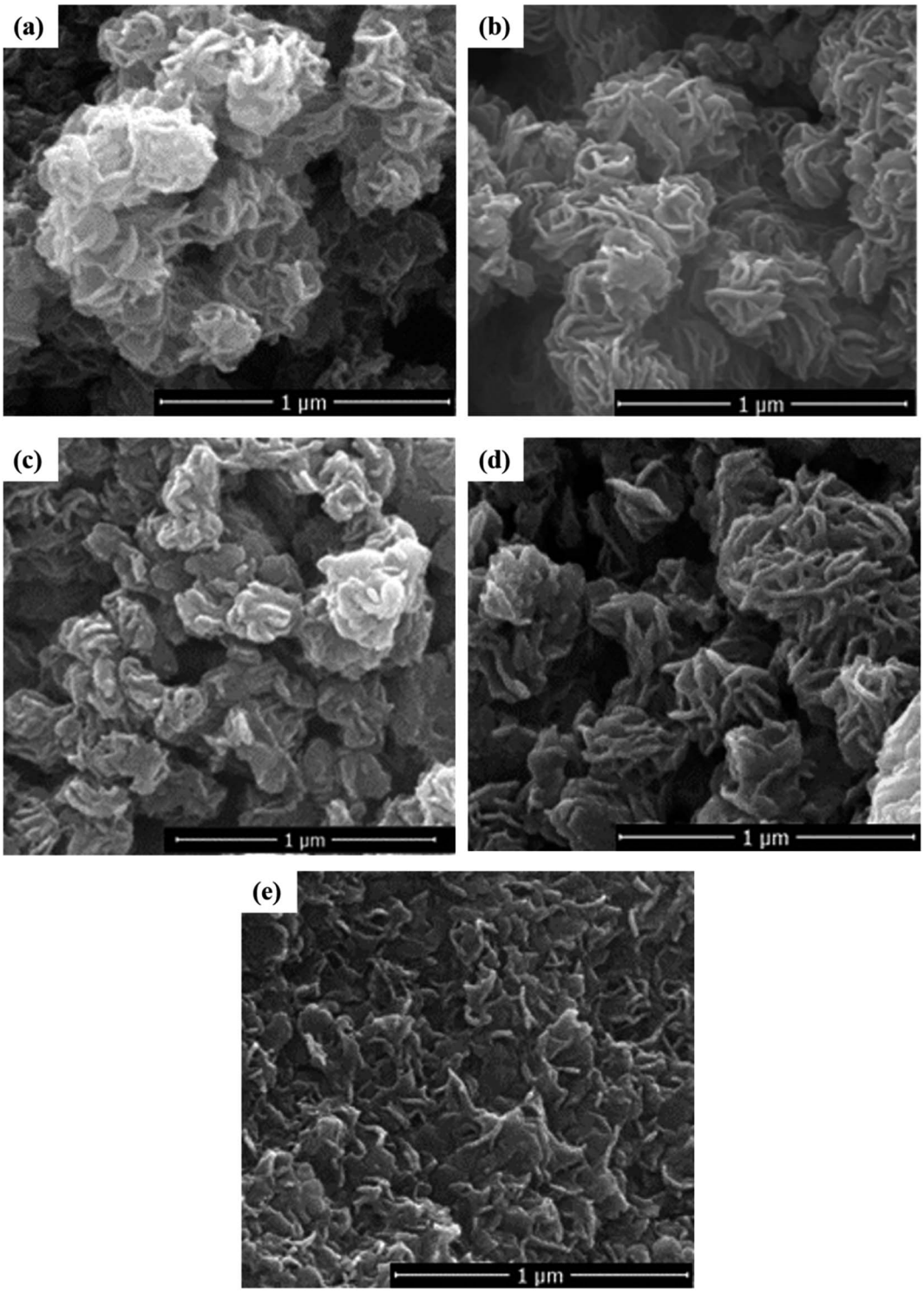

Fig. 3 FESEM images of (a) M, (b) MF, (c) MF-5, (d) MF-3, and (e) MF-1.

3.2. Morphology

Fig. 3 shows the images and morphologies of the synthesized MoS_2 samples. The mechanism of MoS_2 hydrothermal treatment was initialized with the nucleation and crystallization process. This led to the formation of MoS_2 nanosheets, followed by the gradual self-assembly of these nanosheets into a coral structure (Fig. 3a). When F-127 was introduced, the coral structure of MF (Fig. 3b) was less packed compared to that of M. This is because the non-ionic surfactant (F-127) introduced a good dispersing effect, which prevents the particles from clumping together. This hinders the formation of a highly packed structure. Furthermore, the structure of MoS_2 changes drastically from a coral shape to an irregular shape as the pH becomes more acidic. At low pH, the hydroxyl groups on the two hydrophilic tails of the F-127 surfactant are protonated, which creates an electrostatic interaction with the Mo ions.[22] This inhibits the self-assembly process; thus, a random distribution of MoS_2 plate-structures was formed in MF-1 (Fig. 3e).

Fig. 4(a) and (b) show that the HRTEM microstructures of both M and MF are composed of highly dense MoS_2 nanosheets with wrinkled surfaces that are extruded out like lamellar structures. On the other hand, the microstructure of MF-1 (Fig. 4c) is loosely and randomly arranged, which agrees with the FESEM image (Fig. 3e). At higher magnification (Fig. 4d–f), it can be observed that the stacking layer increased in the order of M > MF > MF-1. Additionally, the measured interlayer spacing distances of M, MF and MF-1 are 0.62, 1.09 and 1.51 nm, respectively (inset Fig. 4d–f), which coincides with the *d*-spacing values calculated from XRD. Notably, the low stacking layer of MF-1 is randomly arranged, is oriented in a disorderly fashion and contains a dislocated edge (encircled in Fig. 4f). The presence of F-127 surfactant under very acidic conditions (pH 1) induces greater expansion of the lattice structure along the c-axis and results in the formation of surface defects. This enhances the edge site exposure and thus provides additional catalytic active sites, benefitting the photocatalytic activity. Additionally, MF-1 has lower stacking layers, which can be proved by the greater downward shift of the (002) peak compared with that of M and MF. This is in agreement with Panigrahi and Pathak,[41] who reported that the (002) peak was shifted from 14.0° to 13.4°. Therefore, MF-1 consists of loosely assembled structures, low stacking layers, and a greater number of vertically disordered and defect structures, which signifies that MF-1 demonstrates higher active edge site exposure compared to the other samples.

3.3 Raman spectra

As shown in Fig. 5, the Raman spectra of all the samples possess typical vibration modes of E^1_{2g} (378.3 cm^{-1}) and A^1_g (405.9 cm^{-1}) peaks for MoS_2. This corresponds to the in-plane and out-of-

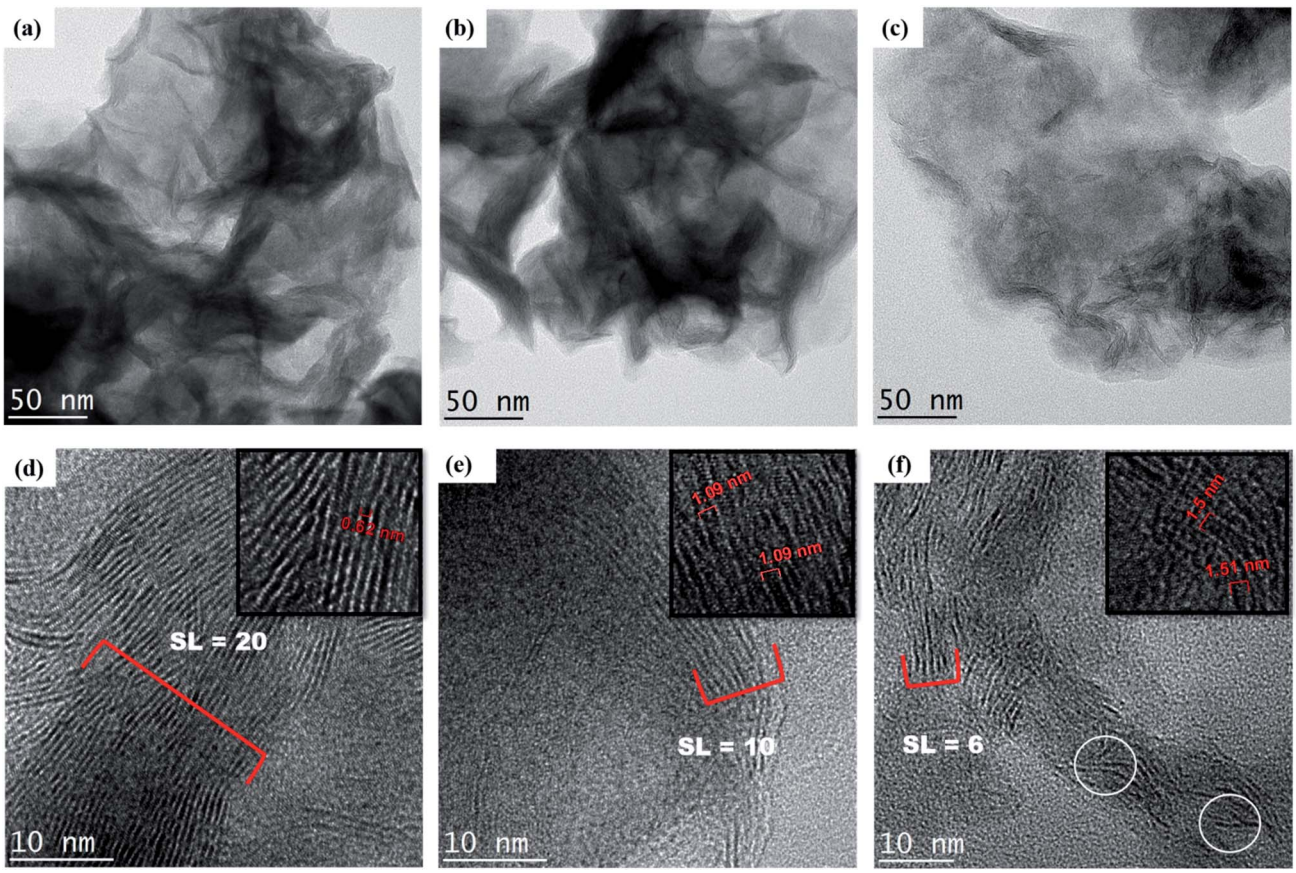

Fig. 4 Low resolution TEM images of (a) M, (b) MF and (c) MF-1 and high resolution TEM images of (d) M, (e) MF and (f) MF-1 with measured stacking layers and interlayer distances (inset).

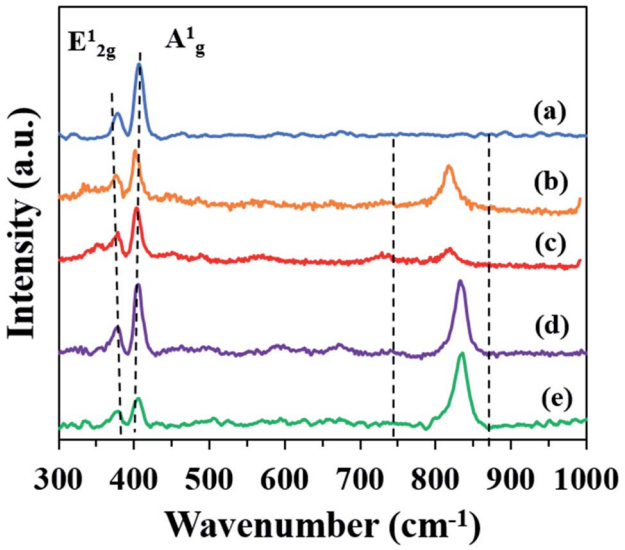

Fig. 5 Raman spectra of (a) M, (b) MF, (c) MF-5, (d) MF-3, and (e) MF-1.

plane vibrations of 2H-MoS_2, respectively.[42] All the samples possess a similar feature, whereby the excitation of the A_{1g} peak mode is higher than the E^2_{1g} peak mode. This indicates that the surfaces of M, MF, MF-5, MF-3 and MF-1 are dominated by the terminated edges.[23] The frequency differences between the E^1_{2g} and A^1_g peaks also provide information regarding the stacking layers.[24,33] The frequency differences between the E^1_{2g} and A^1_g peaks decreased gradually in the order of M > MF > MF-5 > MF-3 > MF-1. This indicates that MF-1 has the fewest stacking layers, as confirmed by the HRTEM results. Moreover, there is an additional peak at ~820 cm^{-1} which is attributed to the bonding of Mo and O atoms[43] in samples MF, MF-5, MF-3 and MF-1. The intensity of the peaks significantly increased when the pH of the synthesis conditions was further lowered. This is due to the oxidation of MoS_2 nanosheets resulting from the expansion of the interlayer spacing.

3.4. Optical properties

Fig. 6a depicts the UV-vis spectra of all the samples, and the tangent line drawn across the figure indicates the absorption edges of the respective samples. It can be observed that the samples have absorption edges within the range of 500 nm to 640 nm. This implies that the samples can be activated under the irradiation of LED light, which possesses a broad light spectrum ranging from 400 to 800 nm (Fig. S1†). Additionally, the measured band gap energy (E_g) of the samples (Fig. 6b) falls within 2.0–2.5 eV, which also indicates that the photocatalytic activity of the samples could be carried out under visible light irradiation. In Fig. 6c, the intensity of the PL decreases in the order of MF-1 > MF-3 > MF > MF-5 > M. This indicates that MF-1 exhibits lower stacking layers, which agrees with other reports.[44,45] In other words, the MoS_2 with lower stacking layers possesses stronger PL intensity, which is attributed to its stronger interaction with the light.[46] Therefore, MF-1 has greater capability to absorb visible light.

As shown in Fig. 6d, the PL peaks for all the samples were deconvoluted into three peaks through a Lorentzian function. The samples are fitted at 1.8, 2.0 and 2.2 eV, which correspond to the A-trions, A-exciton and B-exciton of MoS_2 PL emission, respectively.[21,47] The A-exciton and B-exciton are associated with the excitonic transition at the *K*-point of the Brillouin zone. Meanwhile, the A-trion peak was attributed to the transition resulting from charge impurities in the MoS_2 layer.[48] Technically, non-radiative recombination originating from defects will cause the A and B emission intensities to vary.[49,50] To identify the defect densities, the B/A intensity ratios are recorded in Table 1. Notably, the B/A intensity ratio of MF-1 is ~16% higher than that of M, which indicates that MF-1 possesses greater defects compared to the other samples.

3.5 Chemical composition and elemental states

Fig. 7 shows the XPS measurements of the elemental compositions and the oxidation states of the MoS_2 samples. The Mo 3d spectrum of M consists of a set of doublet peaks which correspond to Mo^{4+} of the Mo $3d_{3/2}$ and Mo $3d_{5/2}$ peaks (Fig. 7a). Meanwhile, the Mo 3d spectra of MF, MF-5, MF-3 and MF-1 (Fig. 7b–e) can be fitted with two doublets. The doublets located at lower binding energies correspond to Mo^{4+} of Mo $3d_{3/2}$ and Mo $3d_{5/2}$, while the smaller doublets located at higher binding energies demonstrate the presence of partially oxidative Mo^{6+}.[51] This further proves the existence of MoS_2 nanosheet oxidation observed in the Raman analysis. The occurrence of different Mo oxidation states indicates the presence of crystal defects in the samples. As for the S 2p peak, samples M, MF, MF-5, MF-3 and MF-1 show similar doublet peaks, attributed to S $2p_{3/2}$ and S $2p_{1/2}$ of S^{2-} for MoS_2 (Fig. 7f–j).

The stoichiometric ratios (S/Mo) of the samples were calculated from the XPS data using the major peak areas of Mo 3d and S 2p, which are assigned to MoS_2. According to Table 1, the S/Mo ratio of M is equal to 2, which corresponds to the pristine MoS_2. However, MF, MF-5, MF-3 and MF-1 possess S/Mo ratios less than 2. This indicates that the samples synthesized in the presence of surfactant and low pH conditions thus contain unsaturated Mo atoms. This condition also implies the presence of S vacancies in samples MF, MF-5, MF-3 and MF-1. Notably, MF-1 has the lowest S : Mo ratio, which indicates that the Mo atoms in MF-1 are highly unsaturated. This is because in an acidic environment, the S atoms in MF-1 can be easily etched, which leads to the formation of Sv sites. Formation of Sv in MoS_2 can cause the electrons to accumulate at the vacancy sites, acting as trapping centers for photogenerated electron–hole pairs.[48] This will induce the formation of A-trions in the PL emissions. However, oxygen and moisture in the atmosphere tend to adsorb on the Sv sites and then act as charge transfer channels. This will remove the excess electrons accumulated at the vacancy sites and thus enhance the PL intensity by subsequently converting the A-trions to A-excitons.[52] This can be observed by the weaker A-trion peak and higher PL intensity of MF-1 compared to the other samples.

Moreover, the unsaturated Mo atoms at the Sv sites of MF, MF-5, MF-3 and MF-1 are highly vulnerable to oxidation in

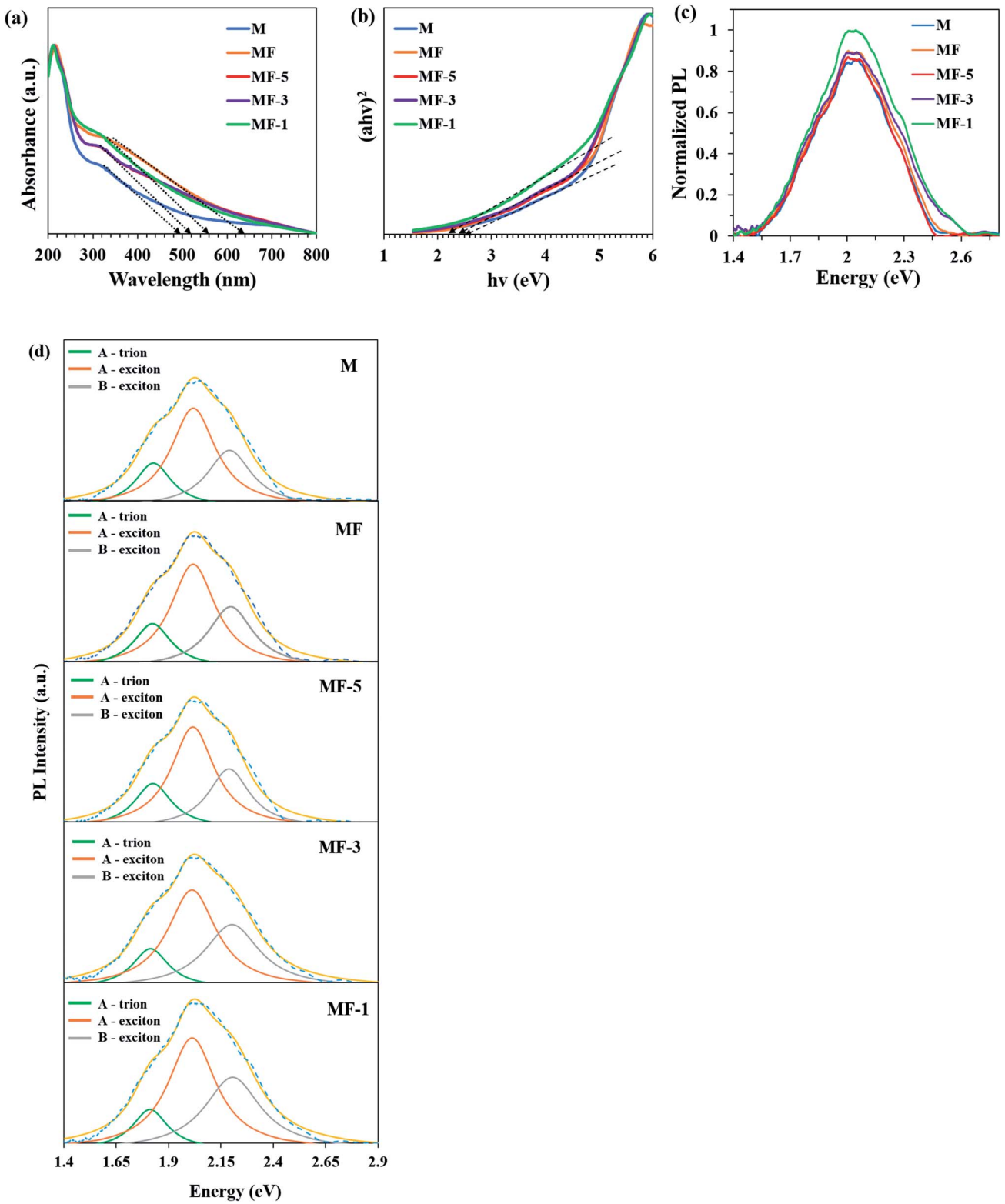

Fig. 6 (a) UV-vis spectra and (b) band gaps of the samples. (c) Normalized PL peaks of the samples. (d) Deconvoluted PL peaks of the samples.

aqueous solution, forming Mo^{6+} species such as $HMoO_4^-$ and MoO_4^{2-}.[53] Additionally, MoO_3 may form due to bonding of O_2 with the Sv sites. Therefore, the Mo^{6+} observed in Mo 3d is assigned to the Mo–O bonding, which is detected in the PL (Fig. 6b).[54] The Mo^{4+}/Mo^{6+} ratios of MF, MF-5, MF-3 and MF-1 decrease with increasing interlayer spacing. The decrease of the Mo^{4+}/Mo^{6+} ratio indicates that more O_2 molecules were adsorbed onto the Sv sites, forming Mo–O bonds. Thus, the presence of Sv provides additional adsorption sites for O_2 molecules through Lewis acid–base interactions. This could

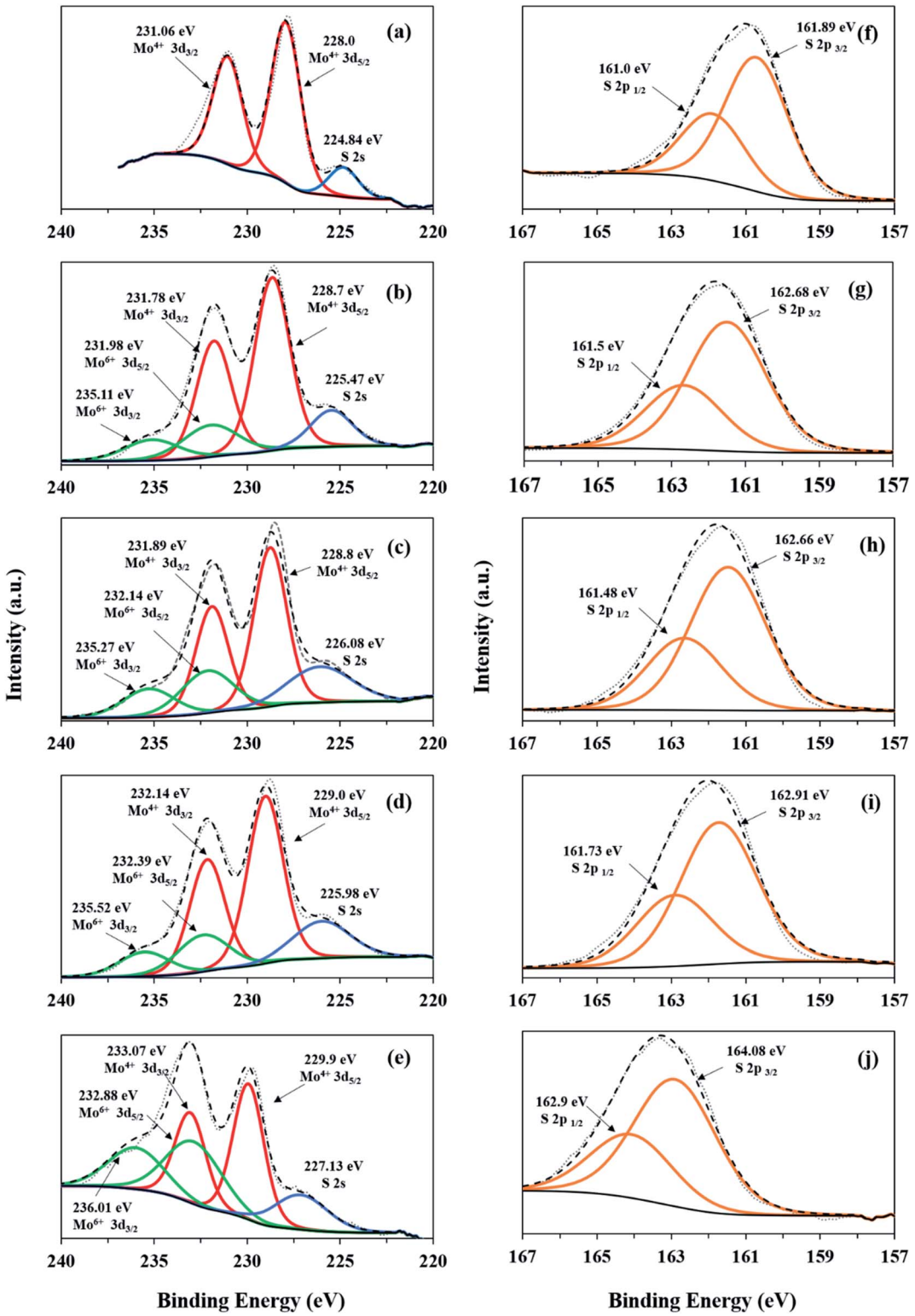

Fig. 7 XPS spectra: Mo 3d and S 2p core level regions of M (a and f), MF (b and g), MF-5 (c and h), MF-3 (d and i), and MF-1 (e and j).

efficiently reduce the O_2 to reactive oxygen species (ROS), such as superoxide radicals ($^{\bullet}O_2^-$).[55] Because MF-1 possesses the lowest Mo^{4+}/Mo^{6+} ratio, MF-1 is capable of forming and weakening O_2 molecules to form ROS species.

3.6 Photodegradation of MB

Fig. 8a shows the photocatalytic activity of the expanded MoS_2 under the illumination of 1 W LED white light. The photolysis of MB dye without the presence of photocatalyst was negligible. It

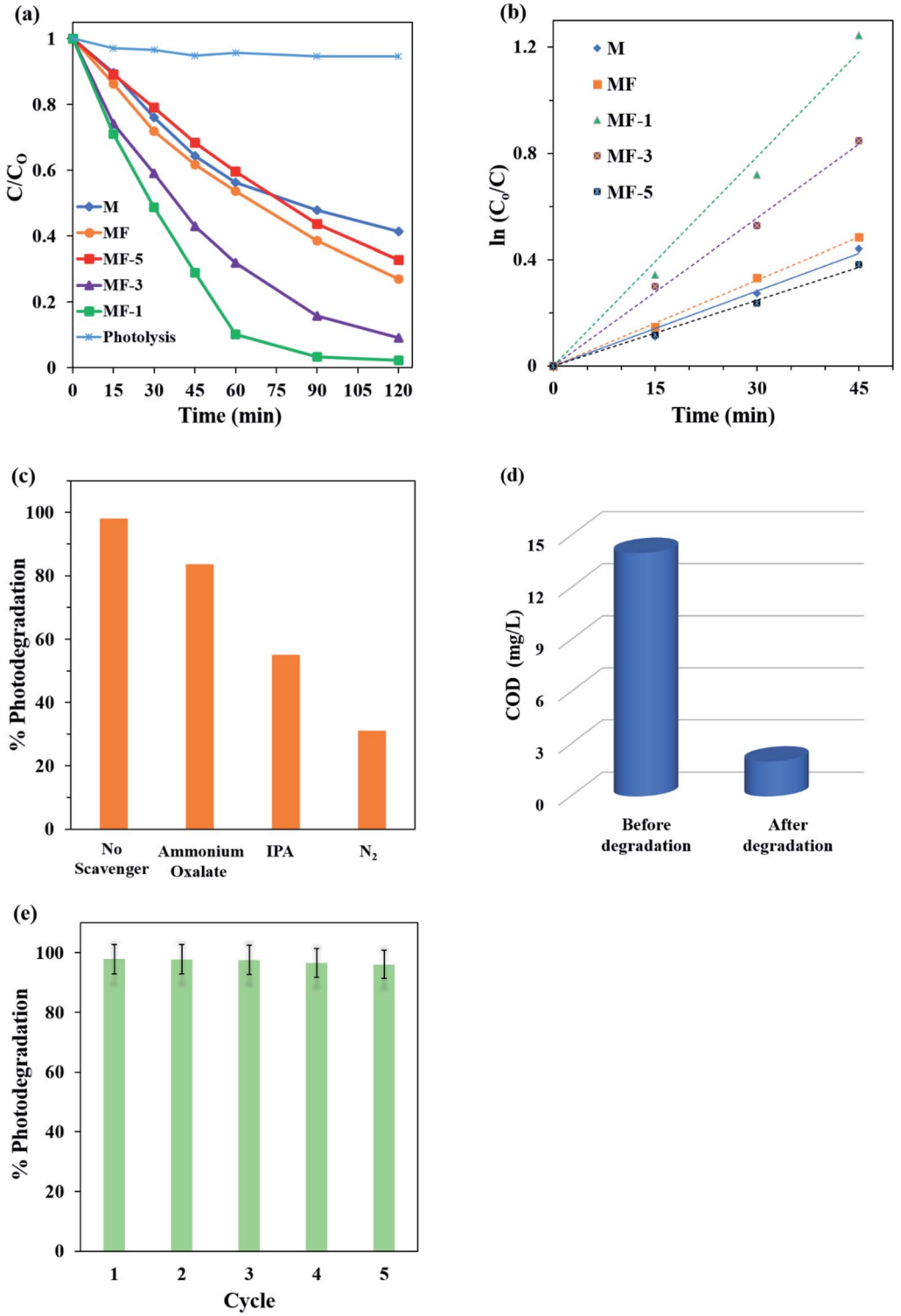

Fig. 8 Comparisons of the (a) photocatalytic performance and (b) pseudo-first-order kinetics of samples M, MF, MF-5 and MF-1. (c) Percentages of photodegradation in the presence of different scavengers. (d) Percentages of COD before and after degradation of MB by MF-1. (e) Recyclability performance of MF-1.

is interesting to observe that MF-1 shows the highest photodegradation of MB dye. MF-1 manages to photodegrade up to 98% of the MB dye within 120 min under LED white light irradiation. The photodegradation activity of the samples decreases as follows: MF-1 ($k = 2.62 \times 10^{-2}$ min^{-1}) > MF-3 (1.85×10^{-2} min^{-1}) > MF (1.08×10^{-2} min^{-1}) > M (9.4×10^{-3} min^{-1}) > MF-5 (8.2×10^{-3} min^{-1}). All the samples are easily activated

under visible LED white light and can photodegrade the dye within 120 min.

According to the Langmuir–Hinshelwood model, the photodegradation process is well fitted with pseudo-first-order kinetics (Fig. 8b). It is noteworthy that the photodegradation of MF is 14% higher than that of M. As expected, the expanded MoS_2 layer of MF has reduced stacking layers; thus, more active edge sites are exposed for photocatalytic activity. However, MF-1 is 39% and 25% more active than M and MF, respectively. This is mainly due to its highly expanded interlayer spaces, which are about 2.4 and 1.38 times higher than those of M and MF. The highly expanded MF-1 has caused the adjacent layers of MoS_2 to decouple, thus causing the individual monolayer to act like a free single MoS_2 layer. Decoupling of the interlayer spacing will occur when the interlayer is highly expanded.[56] The decoupling of the interlayer spacing in MF-1 will increase the edge site exposure, providing more catalytic active sites for the photodegradation of MB dye. Therefore, MF-1 with the largest expansion of interlayer spacing will have the greatest performance in the photocatalytic degradation of MB dye.

The formation of surface defects also served to create additional edge sites for the photocatalytic activity of MF-1. This is because the internal surface of the MoS_2 layer is more accessible, which agrees well with Xie *et al.*[28] They discovered that defects induced additional active edge sites and increased the HER activity by 9 fold. In this study, the presence of Sv in MF-1 facilitated the generation of ROS from O_2. Generally, the adsorption of O_2 on pristine MoS_2 is governed by low adsorption energy, which is insufficient to activate O_2 molecule to form ROS. This is due to its large inactive basal plane surface without Mo dangling bonds.[57] However, surface defects such as cracking and Sv have enhanced the exposure of Mo active metal, providing larger adsorption energy for O_2 molecules. This promotes the migration of electrons from the electron-rich Mo atoms to the adsorbed O_2 molecules, thus generating more ROS such as superoxide radicals ($^{\bullet}O^{2-}$) and hydroxyl radical ($^{\bullet}OH$) for the photodegradation of MB dye. This was proven by Sarkar and co-workers, who showed that MoS_2 that is rich with Mo is highly effective in the generation of ROS.[58] Therefore, the highly expanded interlayer spacing of MF-1 with lower stacking layers, high edge site exposure, rich defects and oxygen passivation of Sv enabled it to possess high photocatalytic activity under LED visible light irradiation.

3.7 Photoelectrochemical (PEC) measurements

Transient photocurrent–time measurements of the samples were performed under the irradiation of visible light with four on–off cycles. As shown in Fig. 9a, all the samples showed instant photocurrent response upon illumination of light that diminished instantly when the light was shut off. This also agrees with a previous study,[59] which implies steady photocatalytic activity. Among the samples, MF-1 depicts the highest photocurrent response without a dramatic reduction even after four consecutive cycles. This proves that MF-1 with highly expanded interlayer spacing has greater photoresponse in generating and separating photogenerated charge carriers. Moreover, in the EIS Nyquist plots (Fig. 9b), MF-1 possesses the smallest arc radius of its semi-circle. This implies that MF-1 experiences the lowest charge transfer resistance. Therefore, MF-1 with low charge transfer resistance and high separation of photogenerated charge manages to enhance the photodegradation of MB dye.

The Mott–Schottky (M–S) plot of MF-1 (Fig. 9c) demonstrates a negative slope, which suggests that MF-1 is a p-type semiconductor. By extrapolating the M–S plot to $1/C^2 = 0$, the flat band potential (E_{FB}) of MF-1 is 0.2 V (V *vs.* Ag/AgCl, pH 6.5). In general, a p-type semiconductor has E_{FB} of approximately 0.3 V above the E_{VB}; thus, the E_{VB} of MF-1 is 0.5 V (*vs.* Ag/AgCl, pH 6.5).[60] Using eqn (6) and (7), the calculated E_{VB} (*vs.* NHE, pH 7) and E_{CB} (*vs.* NHE, pH 7) of MF-1 were +0.7 V and −1.5 V, respectively. Based on these data, the band energy diagram of MF-1 is illustrated in Fig. 10.

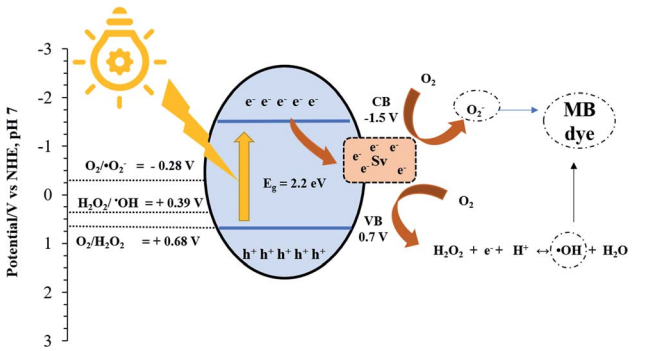

Fig. 10 Schematic of the photodegradation of MB over MF-1.

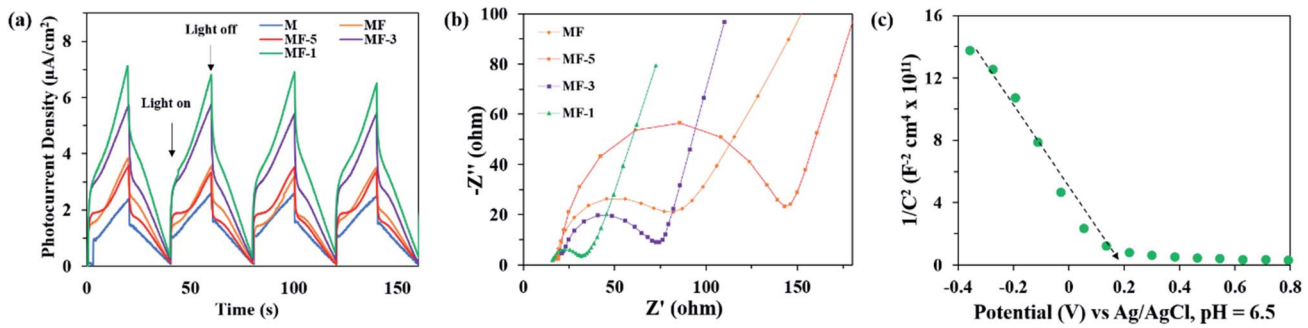

Fig. 9 (a) Transient photocurrent and (b) electron impedance spectroscopy of the samples; (c) Mott–Schottky plot of sample MF-1.

Table 2 Comparative study of the photodegradation activity of MoS_2 materials

Materials	Light source	Dye	Catalyst dosage ($g\ L^{-1}$)	Concentration of dye ($mg\ L^{-1}$)	Degradation percentage (%)	Time taken (min)	Ref.
MoS_2	100 W Xe	MB	0.2	10	89.2	150	59
(1T/2H) MoS_2	400 W W	MO	0.5	20	95	120	60
TiO_2/MoS_2	500 W Xe	RhB	0.1	5	97.8	180	61
$PbBiO_2I/MoS_2$	300 W Xe	RhB	0.3	10	99	180	62
$BiSI/MoS_2$	250 W Mg	CV	0.5	5	90	250	63
$MoS2/Zn_{0.5}Cd_{0.5}S$	300 W Xe	RhB	0.5	10	74	120	64
MoS_2	1 W LED	MB	0.2	20	98	120	This work

3.8 Proposed photodegradation mechanism

Fig. 10 displays the proposed photodegradation mechanism. Upon illumination of light, electrons (e^-) and holes (h^+) are photogenerated on the surface of the MF-1 photocatalyst (eqn (8)). Then, the photogenerated electrons are transferred to the conduction band (CB) and migrate to the Sv sites, which act as trapping sites for the photogenerated electrons. This greatly prevents the photogenerated charges from recombining and thus prolongs the lifespan of the redox reaction. At the Sv sites, the electron-rich Mo atoms possess high adsorption energy with O_2 molecules, which facilitates the reduction of O_2 molecules to $^{\bullet}O_2^-$ radicals [E^0 ($O_2/^{\bullet}O_2^-$) = −0.284 V] (eqn (9)).[58] It is noteworthy that the adsorbed H_2O could not undergo oxidation to form $^{\bullet}OH$ radicals, as the valence band (VB) position of MF-1 (E_{VB} = 0.7 eV) is less positive than the water oxidation potential [E^0 ($^{\bullet}OH/OH^-$) = +2.38 V]. However, the $^{\bullet}OH$ radical can still be generated when the adsorbed O_2 undergoes multi-electron and proton redox reactions (eqn (10) and (11)).[61] The chemical equations involved are described below:

$$\text{MF-1} + h\nu \rightarrow e_{CB}^- + h_{VB}^+ \quad (8)$$

$$O_2 + e^- \rightarrow {}^{\bullet}O_2^- \quad (9)$$

$$O_2 + 2e^- + 2H^+ \rightarrow H_2O_2 \quad (10)$$

$$H_2O_2 + e^- + H^+ \rightarrow {}^{\bullet}OH + H_2O \quad (11)$$

$$^{\bullet}O_2^-, {}^{\bullet}OH, h^+ + \text{MB dye} \rightarrow CO_2 + H_2O + \text{inorganic molecules}$$

In order to verify the proposed mechanism, free radical trapping experiments were conducted using ammonium oxalate and isopropyl alcohol to trap h^+ and $^{\bullet}OH$ radicals, respectively. Pure N_2 was also used as a scavenger and was purged throughout the photocatalytic reaction to restrain the generation of $^{\bullet}O_2^-$ radical.[62] As shown in Fig. 8c, the presence of N_2 gas dramatically decreased the photocatalytic activity to 31%, while in the presence of isopropyl and ammonium oxalate, the photocatalytic activity was reduced to 55% and 83%, respectively. Therefore, this experiment confirmed that $^{\bullet}O_2^-$ radical plays the most important role in the photocatalytic degradation of MB dye, followed by $^{\bullet}OH$ and h^+ radicals. This further justifies that the presence of Sv facilitates the transfer of electrons from MF-1 to O_2 and reduces O_2 to $^{\bullet}O_2^-$ radicals.

Based on Fig. 8d, the COD value of the MB dye solution plummeted from the original value of 14 $mg\ L^{-1}$ to 2 $mg\ L^{-1}$ within 2 h of photocatalytic degradation by MF-1. The 86% COD removal efficiency is sufficient to prove that MF-1 is a promising photocatalyst in the application of dye wastewater treatment. Moreover, the stability of a photocatalyst is an important factor to obtain a highly reusable photocatalyst (Fig. 8e). It can be clearly seen that the photocatalytic degradation does not decelerate dramatically after five consecutive cycles. This indicates that MF-1 is highly stable even after being reused for five cycles. In comparison with previous reported studies (Table 2), highly expanded MoS_2 in our work prove that MoS_2 can acts as photocatalyst with great photocatalytic activity.[65–68] Therefore, it can be concluded that the highly expanded interlayer spaces of MF-1 show remarkable photoactivity by using a more energy-efficient light source and demonstrate high stability.

4. Conclusion

In summary, a highly expanded MoS_2 photocatalyst exhibits high photoactivity under 1 W LED visible light irradiation. The incorporation of F-127 non-ionic surfactant under acidic conditions, especially at pH 1, manages to produce highly expanded MoS_2 with interlayer spaces of 1.51 nm. The exposure of the active edge sites from the highly expanded MF-1 sample has greatly enhanced the photocatalytic performance by 1.7 times compared to pristine MoS_2. Moreover, oxygen passivation of Sv improves the optical absorption of the photocatalyst under the visible light irradiation and enhances the generation of $^{\bullet}O_2^-$ radicals for the photocatalytic reaction. Therefore, due the highly expanded interlayer spacing of MF-1 with high reusability, it could potentially serve as a long-term-usage photocatalyst under energy-efficient LED white light to remove dyes pollutants from wastewater.

Conflicts of interest

There are no conflicts to declare.

Acknowledgements

This study was funded by the University of Malaya under SATU grant (ST011-2018 & ST020-2019) from the University of Malaya.

We also would like to acknowledge National Taipei University of Technology-University of Malaya Joint 5 Research Program (NTUT-UM-109-02) and Ministry of Science and Technology (MOST, 108-2221-E-027-072) for the financial support.

References

1 C. D. Raman and S. Kanmani, Textile dye degradation using nano zero valent iron: A review, *J. Environ. Manage.*, 2016, **177**, 341–355.

2 B. Valley, B. Jing, M. Ferreira and Y. Zhu, Rapid and Efficient Coacervate Extraction of Cationic Industrial Dyes from Wastewater, *ACS Appl. Mater. Interfaces*, 2019, **11**(7), 7472–7478.

3 Sustainable Development Goals (SDG), *Goal 6: Clean water and sanitation*, Retrieved https://www.undp.org/content/undp/en/home/copyright-and-termsofuse.htmlJuly 9, 2020,.

4 L. Liu, Z. Y. Gao, X. P. Su, X. Chen, L. Jiang and J. M. Yao, Adsorption Removal of Dyes from Single and Binary Solutions Using a Cellulose-based Bioadsorbent, *ACS Sustainable Chem. Eng.*, 2015, **3**(3), 432–442.

5 A. D. Liyanage, S. D. Perera, K. Tan, Y. Chabal and K. J. Balkus, Synthesis, Characterization, and Photocatalytic Activity of Y-Doped CeO_2 Nanorods, *ACS Catal.*, 2014, **4**(2), 577–584.

6 R. Javaid and U. Y. Qazi, Catalytic Oxidation Process for the Degradation of Synthetic Dyes: An Overview, *Int. J. Environ. Res. Public Health*, 2019, **16**, 11.

7 A. M. Lotito, U. Fratino, A. Mancini, G. Bergna and C. Di Iaconi, Effective aerobic granular sludge treatment of a real dyeing textile wastewater, *Int. Biodeterior. Biodegrad.*, 2012, **69**, 62–68.

8 Y. Wang, X. Ye, G. Chen, D. Li, S. Meng and S. Chen, Synthesis of $BiPO_4$ by crystallization and hydroxylation with boosted photocatalytic removal of organic pollutants in air and water, *J. Hazard. Mater.*, 2020, **399**, 122999.

9 M. T. L. Lai, C. W. Lai, K. M. Lee, S. W. Chook, T. C. K. Yang, S. H. Chong and J. C. Juan, Facile one-pot solvothermal method to synthesize solar active Bi_2WO_6 for photocatalytic degradation of organic dye, *J. Alloys Compd.*, 2019, **801**, 502–510.

10 N. Rahimi, R. A. Pax and E. M. Gray, Review of functional titanium oxides. I: TiO_2 and its modifications, *Prog. Solid State Chem.*, 2016, **44**(3), 86–105.

11 W.-K. Jo and R. J. Tayade, New Generation Energy-Efficient Light Source for Photocatalysis: LEDs for Environmental Applications, *Ind. Eng. Chem. Res.*, 2014, **53**(6), 2073–2084.

12 D. Wu, W. Wang, T. W. Ng, G. Huang, D. Xia, H. Y. Yip, H. K. Lee, G. Li, T. An and P. K. Wong, Visible-light-driven photocatalytic bacterial inactivation and the mechanism of zinc oxysulfide under LED light irradiation, *J. Mater. Chem. A*, 2016, **4**(3), 1052–1059.

13 K. Dai, L. Lu, J. Dong, Z. Ji, G. Zhu, Q. Liu, Z. Liu, Y. Zhang, D. Li and C. Liang, Facile synthesis of a surface plasmon resonance-enhanced Ag/AgBr heterostructure and its photocatalytic performance with 450 nm LED illumination, *Dalton Trans.*, 2013, **42**(13), 4657–4662.

14 Q. Ou, S. Xu, Y. Long and X. Zhang, Porous visible light-responsive Fe^{3+}-doped carbon nitride for efficient degradation of sulfadiazine, *Environ. Sci. Pollut. Res.*, 2020, **27**(22), 27849–27858.

15 K. C. Devarayapalli, S. V. Prabhakar Vattikuti, T. V. Madhukar Sreekanth, P. Chidanandha Nagajyothi and J. Shim, Pyrolysis-Synthesized g-C_3N_4/Nb_2O_5 Nanocomposite for Enhanced Photocatalytic Activity under White LED Light Irradiation, *ChemistrySelect*, 2019, **4**(45), 13250–13258.

16 Z. Li, X. Meng and Z. Zhang, Recent development on MoS_2-based photocatalysis: A review, *J. Photochem. Photobiol., C*, 2018, **35**, 39–55.

17 Z. Liang, R. Shen, Y. H. Ng, P. Zhang, Q. Xiang and X. Li, A review on 2D MoS_2 cocatalysts in photocatalytic H_2 production, *J. Mater. Sci. Technol.*, 2020, **56**, 89–121.

18 Y. Liu, Y. Xie, L. Liu and J. Jiao, Sulfur vacancy induced high performance for photocatalytic H_2 production over 1T@2H phase MoS_2 nanolayers, *Catal. Sci. Technol.*, 2017, **7**(23), 5635–5643.

19 Y. Okuno, O. Lancry, A. Tempez, C. Cairone, M. Bosi, F. Fabbri and M. Chaigneau, Probing the nanoscale light emission properties of a CVD-grown MoS_2 monolayer by tip-enhanced photoluminescence, *Nanoscale*, 2018, **10**(29), 14055–14059.

20 G. Deokar, N. S. Rajput, P. Vancso, F. Ravaux, M. Jouiad, D. Vignaud, F. Cecchet and J. F. Colomer, Large area growth of vertically aligned luminescent MoS_2 nanosheets, *Nanoscale*, 2017, **9**(1), 277–287.

21 G. Pradhan and A. K. Sharma, Anomalous Raman and photoluminescence blue shift in mono- and a few layered pulsed laser deposited MoS_2 thin films, *Mater. Res. Bull.*, 2018, **102**, 406–411.

22 M. Li, D. Wang, J. Li, Z. Pan, H. Ma, Y. Jiang, Z. Tian and A. Lu, Surfactant-assisted hydrothermally synthesized MoS_2 samples with controllable morphologies and structures for anthracene hydrogenation, *Chin. J. Catal.*, 2017, **38**(3), 597–606.

23 H. Wang, Z. Lu, D. Kong, J. Sun, T. M. Hymel and Y. Cui, Electrochemical Tuning of MoS_2 Nanoparticles on Three-Dimensional Substrate for Efficient Hydrogen Evolution, *ACS Nano*, 2014, **8**, 5.

24 Y. C. Dong, S.-K. Park, Y.-H. Chung, S.-H. Yu, D.-H. Lim, N. Jung, H. C. Ham, H.-Y. Park, Y. Piao, S. J. Yoo and Y.-E. Sung, Edge-exposed MoS_2 nano-assembled structures as efficient electrocatalysts for hydrogen evolution reaction, *Nanoscale*, 2014, **6**, 2131–2136.

25 H. K. Sadhanala, S. Senapati, K. V. Harika, K. K. Nanda and A. Gedanken, Green synthesis of MoS_2 nanoflowers for efficient degradation of methylene blue and crystal violet dyes under natural sun light conditions, *New J. Chem.*, 2018, **42**(17), 14318–14324.

26 J. Kibsgaard, Z. Chen, B. N. Reinecke and T. F. Jaramillo, Engineering the surface structure of MoS2 to preferentially expose active edge sites for electrocatalysis, *Nat. Mater.*, 2012, **11**(11), 963–969.

27 C. G. Morales-Guio and X. Hu, Amorphous molybdenum sulfides as hydrogen evolution catalysts, *Acc. Chem. Res.*, 2014, **47**(8), 2671–2681.

28 J. Xie, H. Zhang, S. Li, R. Wang, X. Sun, M. Zhou, J. Zhou, X. W. Lou and Y. Xie, Defect-rich MoS_2 ultrathin nanosheets with additional active edge sites for enhanced electrocatalytic hydrogen evolution, *Adv. Mater.*, 2013, **25**(40), 5807–5813.

29 M. R. Gao, M. K. Chan and Y. Sun, Edge-terminated molybdenum disulfide with a 9.4-A interlayer spacing for electrochemical hydrogen production, *Nat. Commun.*, 2015, **6**, 7493.

30 M. Lin, G. Huang, W. Chen, Z. Wang, J. Ye, H. Li, D. Chen and J. Y. Lee, Cationic surfactant-assisted hydrothermal synthesis of few-layer molybdenum disulfide/graphene composites: Microstructure and electrochemical lithium storage, *J. Power Sources*, 2014, **264**, 262–271.

31 Q. Liu, X. Li, Q. He, A. Khalil, D. Liu, T. Xiang, X. Wu and L. Song, Gram-Scale Aqueous Synthesis of Stable Few-Layered 1T-MoS_2 : Applications for Visible-Light-Driven Photocatalytic Hydrogen Evolution, *Small*, 2015, **11**(41), 5556–5564.

32 J. Zhou, G. Fang, A. Pan and S. Liang, Oxygen-Incorporated MoS_2 Nanosheets with Expanded Interlayers for Hydrogen Evolution Reaction and Pseudocapacitor Applications, *ACS Appl. Mater. Interfaces*, 2016, **8**(49), 33681–33689.

33 X. Zeng, L. Niu, L. Song, X. Wang, X. Shi and J. Yan, Effect of Polymer Addition on the Structure and Hydrogen Evolution Reaction Property of Nanoflower-Like Molybdenum Disulfide, *Metals*, 2015, **5**(4), 1829–1844.

34 J. Shao, Q. Qu, Z. Wan, T. Gao, Z. Zuo and H. Zheng, From Dispersed Microspheres to Interconnected Nanospheres: Carbon-Sandwiched Monolayered MoS_2 as High-Performance Anode of Li-Ion Batteries, *ACS Appl. Mater. Interfaces*, 2015, **7**, 22927–22934.

35 R. M. Mohamed and F. A. Harraz, Mechanistic investigation and photocatalytic activity of yttrium vanadate (YVO_4) nanoparticles for organic pollutants mineralization, *J. Mater. Res. Technol.*, 2020, **9**(3), 5666–5675.

36 T. Giannakopoulou, I. Papailias, N. Todorova, N. Boukos, Y. Liu, J. Yu and C. Trapalis, Tailoring the energy band gap and edges' potentials of g-C_3N_4/TiO_2 composite photocatalysts for NO_x removal, *Chem. Eng. J.*, 2017, **310**, 571–580.

37 B. Mao, B. Wang, F. Yu, K. Zhang, Z. Zhang, J. Hao, J. Zhong, Y. Liu and W. Shi, Hierarchical MoS_2 nanoflowers on carbon cloth as an efficient cathode electrode for hydrogen evolution under all pH values, *Int. J. Hydrogen Energy*, 2018, **43**, 11038–11046.

38 J. Shao, Q. Qu, Z. Wan, T. Gao, Z. Zuo and H. Zheng, From Dispersed Microspheres to Interconnected Nanospheres: Carbon-Sandwiched Monolayered MoS_2 as High-Performance Anode of Li-Ion Batteries, *ACS Appl. Mater. Interfaces*, 2015, **7**(41), 22927–22934.

39 H. Dong, Y. Xu, C. Zhang, Y. Wu, M. Zhou, L. Liu, Y. Dong, Q. Fu, M. Wu and Y. Lei, MoS_2 nanosheets with expanded interlayer spacing for enhanced sodium storage, *Inorg. Chem. Front.*, 2018, **5**(12), 3099–3105.

40 J. Chen, Y. Xia and J. Yang, Graphene/surfactant-assisted synthesis of edge-terminated molybdenum disulfide with enlarged interlayer spacing, *Mater. Lett.*, 2018, **210**, 248–251.

41 P. K. Panigrahi and A. Pathak, Aqueous Medium Synthesis Route for Randomly Stacked Molybdenum Disulfide, *J. Nanopart.*, 2013, **2013**, 1–10.

42 J. G. Kim, W. S. Yun, S. Jo, J. D. Lee and C.-H. Cho, Effect of interlayer interactions on exciton luminescence in atomic-layered MoS_2 crystals, *Sci. Rep.*, 2016, **6**, 1.

43 S. Hussain, J. Singh, D. Vikraman, A. K. Singh, M. Z. Iqbal, M. F. Khan, P. Kumar, D. C. Choi, W. Song, K. S. An, J. Eom, W. G. Lee and J. Jung, Large-area, continuous and high electrical performances of bilayer to few layers MoS_2 fabricated by RF sputtering *via* post-deposition annealing method, *Sci. Rep.*, 2016, **6**, 30791.

44 M. A. Islam, J. Church, C. Han, H. S. Chung, E. Ji, J. H. Kim, N. Choudhary, G. H. Lee, W. H. Lee and Y. Jung, Noble metal-coated MoS_2 nanofilms with vertically-aligned 2D layers for visible light-driven photocatalytic degradation of emerging water contaminants, *Sci. Rep.*, 2017, **7**(1), 14944.

45 S. Catalán-Gómez, S. Garg, A. Redondo-Cubero, N. Gordillo, A. de Andrés, F. Nucciarelli, S. Kim, P. Kung and J. L. Pau, Photoluminescence enhancement of monolayer MoS_2 using plasmonic gallium nanoparticles, *Nanoscale Adv.*, 2019, **1**(2), 884–893.

46 S. Catalán-Gómez, S. Garg, A. Redondo-Cubero, N. Gordillo, A. de Andrés, F. Nucciarelli, S. Kim, P. Kung and J. L. Pau, Photoluminescence enhancement of monolayer MoS_2 using plasmonic gallium nanoparticles, *Nanoscale Adv.*, 2019, **1**, 884–893.

47 M. R. Habib, H. Li, Y. Kong, T. Liang, S. M. Obaidulla, S. Xie, S. Wang, X. Ma, H. Su and M. Xu, Tunable photoluminescence in a van der Waals heterojunction built from a MoS_2 monolayer and a PTCDA organic semiconductor, *Nanoscale*, 2018, **10**(34), 16107–16115.

48 L. P. L. Mawlong, K. K. Paul and P. K. Giri, Direct Chemical Vapor Deposition Growth of Monolayer MoS_2 on TiO_2 Nanorods and Evidence for Doping-Induced Strong Photoluminescence Enhancement, *J. Phys. Chem. C*, 2018, **122**, 15017–15025.

49 K. M. McCreary, A. T. Hanbicki, S. V. Sivaram and B. T. Jonker, A- and B-exciton photoluminescence intensity ratio as a measure of sample quality for transition metal dichalcogenide monolayers, *APL Mater.*, 2018, **6**, 111106.

50 T. Verhagen, V. L. P. Guerra, G. Haider, M. Kalbac and J. Vejpravova, Towards the evaluation of defects in MoS_2 using cryogenic photoluminescence spectroscopy, *Nanoscale*, 2020, **12**, 3019–3028.

51 W. Su, P. Wang, Z. Cai, J. Yang and X. Wang, One-pot hydrothermal synthesis of Al-doped MoS_2@graphene aerogel nanocomposite electrocatalysts for enhanced hydrogen evolution reaction, *Results Phys.*, 2019, **12**, 250–258.

52 L. Xu, L. Zhao, Y. Wang, M. Zou, Q. Zhang and A. Cao, Analysis of photoluminescence behavior of high-quality single-layer MoS_2, *Nano Res.*, 2019, **12**(7), 1619–1624.

53 W. T. Yein, Q. Wang, Y. Liu, Y. Li, J. Jian and X. Wu, Piezo-potential induced molecular oxygen activation of defect-rich MoS_2 ultrathin nanosheets for organic dye degradation in dark, *J. Environ. Chem. Eng.*, 2020, **8**(1), 103626.

54 H. Nan, Z. Wang, W. Wang, Z. Liang, Y. Lu, Q. Chen, D. He, P. Tan, F. Miao, X. Wang, J. Wang and Z. Ni, Strong Photoluminescence Enhancement of MoS_2 through Defect Engineering and Oxygen Bonding, *ACS Nano*, 2014, **8**(6), 5738–5745.

55 Y. Zheng, Z. Yu, H. Ou, A. M. Asiri, Y. Chen and X. Wang, Black Phosphorus and Polymeric Carbon Nitride Heterostructure for Photoinduced Molecular Oxygen Activation, *Adv. Funct. Mater.*, 2018, **28**(10), 1705407.

56 Y. Zhang, H. Li, H. Wang, R. Liu, S.-L. Zhang and Z.-J. Qiu, On Valence-Band Splitting in Layered MoS_2, *ACS Nano*, 2015, **9**(8), 8514–8519.

57 B. B. Xiao, P. Zhang, L. P. Han and Z. Wen, Functional MoS_2 by the Co/Ni doping as the catalyst for oxygen reduction reaction, *Appl. Surf. Sci.*, 2015, **354**, 221–228.

58 D. Sarkar, B. Mondal, A. Som, S. J. Ravindran, S. K. Jana, C. K. Manju and T. Pradeep, Holey MoS_2 Nanosheets with Photocatalytic Metal Rich Edges by Ambient Electrospray Deposition for Solar Water Disinfection, *Global Challenges*, 2018, **2**(12), 1800052.

59 H. Qin, R. T. Guo, X. Y. Liu, W. G. Pan, Z. Y. Wang, X. Shi, J. Y. Tang and C. Y. Huang, Z-Scheme MoS_2/g-C_3N_4 heterojunction for efficient visible light photocatalytic CO_2 reduction, *Dalton Trans.*, 2018, **47**(42), 15155–15163.

60 W. Yin, L. Bai, Y. Zhu, S. Zhong, L. Zhao, Z. Li and S. Bai, Embedding Metal in the Interface of a p–n Heterojunction with a Stack Design for Superior Z-Scheme Photocatalytic Hydrogen Evolution, *ACS Appl. Mater. Interfaces*, 2016, **8**(35), 23133–23142.

61 T. B. Nguyen and R.-a. Doong, Fabrication of highly visible-light-responsive $ZnFe_2O_4$/TiO_2 heterostructures for the enhanced photocatalytic degradation of organic dyes, *RSC Adv.*, 2016, **6**(105), 103428–103437.

62 Y. Deng, L. Tang, G. Zeng, C. Feng, H. Dong, J. Wang, H. Feng, Y. Liu, Y. Zhou and Y. Pang, Plasmonic resonance excited dual Z-scheme $BiVO_4$/Ag/Cu_2O nanocomposite: synthesis and mechanism for enhanced photocatalytic performance in recalcitrant antibiotic degradation, *Environ. Sci.: Nano*, 2017, **4**(7), 1494–1511.

63 Z. Zhou, Y. Lin, P. Zhang, E. Ashalley, M. Shafa, H. Li, J. Wu and Z. Wang, Hydrothermal fabrication of porous MoS_2 and its visible light photocatalytic properties, *Mater. Lett.*, 2014, **131**, 122–124.

64 M. R. Saber, G. Khabiri, A. A. Maarouf, M. Ulbricht and A. S. G. Khalil, A comparative study on the photocatalytic degradation of organic dyes using hybridized 1T/2H, 1T/3R and 2H MoS_2 nano-sheets, *RSC Adv.*, 2018, **8**(46), 26364–26370.

65 C. Wang, H. Lin, Z. Liu, J. Wu, Z. Xu and C. Zhang, Controlled Formation of TiO_2/MoS_2 Core-Shell Heterostructures with Enhanced Visible-Light Photocatalytic Activities, *Part. Part. Syst. Charact.*, 2016, **33**(4), 221–227.

66 M. Li, S. Yin, T. Wu, J. Di, M. Ji, B. Wang, Y. Chen, J. Xia and H. Li, Controlled preparation of MoS_2/$PbBiO_2I$ hybrid microspheres with enhanced visible-light photocatalytic behaviour, *J. Colloid Interface Sci.*, 2018, **517**, 278–287.

67 S. Bargozideh and M. Tasviri, Construction of a novel BiSI/MoS_2 nanocomposite with enhanced visible-light driven photocatalytic performance, *New J. Chem.*, 2018, **42**(22), 18236–18241.

68 X.-L. Yin, S.-R. Han and L.-L. Li, MoS_2/$Zn_{0.5}Cd_{0.5}S$ hierarchical nano-heterostructure for efficient light absorption and photocatalytic pollution degradation, *Optik*, 2020, **212**, 164680.